



Understanding the Benefit of Hybrid Electrolytes towards Vanadium Dissolution Suppression and Improved Capacity Retention in Zinc-Aqueous Batteries Using NaV_3O_8 Cathodes

Andrew Nicoll, Gupreet Singh, Ryan C. Hill, Patrick J. Barry, Esther S. Takeuchi, Lu Ma, Daniel Olds, Lisa M. Housel, Amy C. Marschilok, Shan Yan,* and Kenneth J. Takeuchi*

Vanadate cathodes used in aqueous Zn-ion batteries with ZnSO_4 are hindered by capacity loss from V dissolution into the electrolyte. However, studies pinpointing the onset of dissolution as a function of electrochemical redox state and quantifying the amount of associated active material are lacking. To prevent dissolution of the NaV_3O_8 active material, Na^+ ions are introduced into the electrolyte. Specifically, a hybrid $\text{ZnSO}_4 + \text{Na}_2\text{SO}_4$ electrolyte is investigated in concert with NaV_3O_8 (NVO) cathodes of varied crystallinity to determine the resulting impacts on cathode dissolution and functional electrochemistry. The use of Na^+ -containing hybrid electrolyte shows no significant change in Zn^{2+} diffusion coefficients yet improved capacity retention.

Time-resolved quantitative optical emission spectroscopy demonstrates the suppression of V dissolution with the hybrid electrolyte in both pristine and cycled electrodes. *Operando* synchrotron X-ray diffraction and absorption provide mechanistic insights. Hydrated NVO with wider interplanar spacing exhibits much higher $\text{H}^+/\text{Zn}^{2+}$ capacity, while the Na_2SO_4 mitigates the formation of irreversible side products. This study demonstrates that the use of hybrid electrolytes and control of crystallite size in the parent material can significantly improve electrochemical behavior of layered V-based cathodes in Zn-ion batteries, providing a general strategy toward safe and resilient aqueous battery systems.

1. Introduction

Lithium-ion batteries have dominated the consumer electronics and automobile market with desirable cycle life and high-energy

density. However, due to the relatively high cost and demand for lithium, along with concerns over the volatility and toxicity of organic electrolytes, aqueous Zn-ion batteries (AZIBs) have recently gained significant interest for applications where lower cost and improved safety are more desirable over energy density.^[1–5] Vanadium oxides have a rich structural diversity^[6–11] and are conceptually appealing due to high theoretical capacities based on opportunity for multiple electron transfers per formula unit ($\text{V}^{5+} \rightarrow \text{V}^{4+} \rightarrow \text{V}^{3+}$) within a desirable voltage window. Some of the well-suited cathode systems for zinc-ion batteries are layered vanadate materials,^[12–15] including sodium vanadium oxide (NVO),^[16,17] which offers fast transport and specific capacities over 300 mAh g⁻¹ with high coulombic efficiency ($\approx 99\%$).^[18–24] Mildly acidic aqueous Zn-ion electrolytes like ZnSO_4 are desirable due to their low cost and environmentally benign character; however, they can also contribute to irreversible V dissolution, which over time results in capacity fade in cells with NVO-based cathodes.^[25,26] Reported attempts at suppressing dissolution in vanadate cathodes have included the use of hybrid inorganic solid–liquid electrolytes,^[27] incorporating alternative metals as interlayer ions (La^{3+} , Ba^{2+}),^[28,29] “water-in-salt” ZnCl_2 electrolyte,^[30] polyaniline structure stabilizers,^[31] fluorinated Zn salts like $\text{Zn}(\text{OTf})_2$,^[32] deposition of MXenes on vanadate surfaces,^[33,34] atomic-layer deposition on the cathode surface,^[35,36] and a sodium pre-intercalated vanadium oxide/carbon (VO/LSC) composite using sustainable sodium lignosulfonate as both a carbon and sodium source.^[37] While showing notable benefits in terms of electrochemical function, many of these approaches have

A. Nicoll, G. Singh, R. C. Hill, P. J. Barry, E. S. Takeuchi, A. C. Marschilok, S. Yan, K. J. Takeuchi

Institute of Sustainability, Electrification, and Energy (ISEE)

Stony Brook University

Stony Brook, NY 11794, USA

E-mail: syan@bnl.gov

kenneth.takeuchi.1@stonybrook.edu

A. Nicoll, G. Singh, P. J. Barry, E. S. Takeuchi, A. C. Marschilok, K. J. Takeuchi

Department of Chemistry

Stony Brook University

Stony Brook, NY 11794, USA

E. S. Takeuchi, A. C. Marschilok, K. J. Takeuchi

Department of Materials Science and Chemical Engineering

Stony Brook University

Stony Brook, NY 11794, USA

E. S. Takeuchi, L. M. Housel, A. C. Marschilok, S. Yan, K. J. Takeuchi

Interdisciplinary Science Department

Brookhaven National Laboratory

Upton, NY 11973, USA

L. Ma, D. Olds

National Synchrotron Light Source II

Brookhaven National Laboratory

Upton, NY 11973, USA



Supporting information for this article is available on the WWW under <https://doi.org/10.1002/batt.202500036>

inherent drawbacks such as increased complexity of the vanadate structure (alternate cation incorporation), complex and expensive synthesis techniques (atomic-layer deposition), and introduction of an additional component onto the cathode (MXene and polyaniline matrices). Another approach is the use of electrolyte additives, which are known to be effective at improving long-term stability in AZIBs by mitigating failure modes such as Zn corrosion, Zn dendrites, hydrogen evolution reaction, and cathode material dissolution. Additives with high water solubility, compatibility with the primary salt in the electrolyte, cost-effectiveness, and low toxicity are desirable.

The use of hybrid electrolytes prepared with sodium-based salts is a straightforward approach to add beneficial properties to the AZIB system.^[38] The NVO structure consists of V_3O_8 layers bolstered by Na^+ ions pillars interacting with O atoms in the VO_6 interlayer space. Conceptually, introduction of Na^+ in the electrolyte could be an effective means of suppressing V dissolution by limiting Na solubility from the cathode into the electrolyte, preserving the Na–O interactions, which in turn should help preserve the cathode structure and capacity over long-term cycling. The utilization of Na salts as an additive has been shown to improve cycling stability via uniform deposition of Zn as well as suppress cathode dissolution in an AZIB with a Na^+ pre-inserted manganese oxide cathode.^[24,25,39–41]

The phenomenon of capacity fade due to the dissolution of vanadium-based compounds in electrolytes during cycling was recently identified to be a key barrier limiting the implementation of vanadium-based materials for high-energy aqueous zinc-ion batteries.^[42] While improved capacity retention with cycling upon addition of Na^+ to the electrolyte has been previously reported as noted above, studies pinpointing the onset of dissolution as a function of electrochemical redox state and quantifying the amount of dissolution are lacking. Herein, the kinetics of V dissolution were quantitatively determined for different NVO materials and different electrolytes within aqueous zinc-ion batteries. Specifically, NVO materials of varied water content and crystallite sizes were synthesized and characterized and investigated with two electrolytes, 1.0 M $ZnSO_4$ (ZS) and 0.5 M Na_2SO_4 + 0.5 M $ZnSO_4$ (HYB), to correlate differences in dissolution properties with differences in electrochemical cycling capacity retention. ICP-OES was used to determine the dissolution kinetics of V from NVO in the ZS and HYB electrolytes. *Operando* X-ray powder diffraction (XPD) and X-ray absorption spectroscopy (XAS) were

performed on Zn/NVO cells to provide insights into structure, oxidation state, and coordination of V in NVO cathodes as a function of the NVO material type and electrolyte composition.

2. Results and Discussion

2.1. Materials Characterization

Following synthesis and annealing, structural parameters for the h-NVO, NVO(300), and NVO(500) powders contained in the 3D, self-supporting NVO-based electrodes were resolved using Rietveld refinement of diffraction patterns. Calculated refinement patterns are shown in Figure 1A–C, and tabular data are given in Table S1, Supporting Information. The broad, low-intensity background feature from $2\theta = 2.5$ degrees to $2\theta = 3.5$ degrees is from the MWCNT matrix. The (100) interplanar-distance, along which the V_3O_8 layers, is stacked and decreased with increasing annealing temperature: 7.81 Å in h-NVO to 6.99 Å in NVO(300) and 6.96 Å in NVO(500). The calculated crystallite size along the 100 axis was 11.1(4) nm for h-NVO, 11.3(30) nm for NVO(300), and 51(1) nm for NVO(500). As shown in Figure S1, Supporting Information, water content using TGA analysis was determined to be 7.7%, 2.5%, and 0.8%, respectively. ICP-OES analysis was used to determine the Na to V ratio in h-NVO, NVO(300), and NVO(500) powders. Consequently, the molecular formulas and formula masses of the three NVO powders were determined to be $Na_{1.15}V_3O_8 \cdot 1.65H_2O$, $Na_{1.13}V_3O_8 \cdot 0.44H_2O$, and $Na_{1.15}V_3O_8 \cdot 0.14H_2O$ for h-NVO, NVO(300), and NVO(500), respectively.

Annealing to 300 °C primarily results in removal of structural water and an accompanying decrease in interlayer spacing, while increasing the annealing temperature to 500 °C results in an increased crystallite size. Interlayer spacing is not significantly affected by increasing the annealing temperature. These observations are consistent with previous reports on the effects of annealing NVO at 300 and 500 °C.^[18,19] The preservation of the stoichiometric Na to V ratios during annealing will allow elucidation of changes in charge storage characteristics based on differences in water content, interlayer spacing and crystallite sizes.

The X-ray absorption spectra (XAS) at the X-ray absorption near-edge structure (XANES) region of the V K-edge for synthesized h-NVO, NVO-300, and NVO-500 materials are shown in Figure S2, Supporting Information. The oxidation states for V were

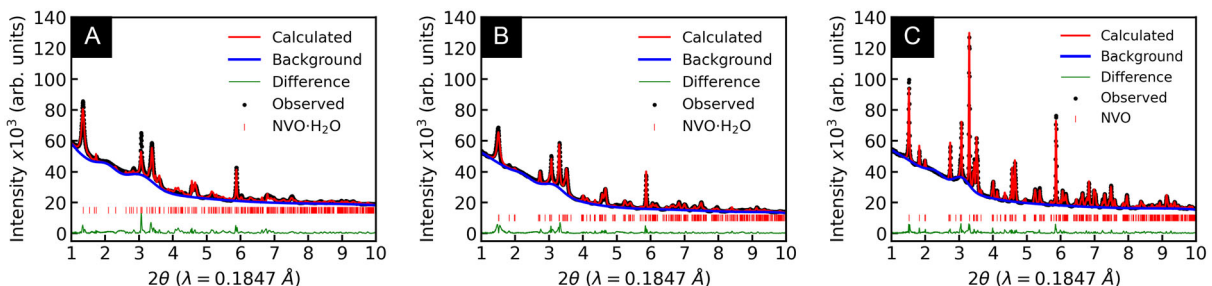


Figure 1. Rietveld refinement of A) h-NVO, B) NVO(300), and C) NVO(500) electrodes. R_{wp} values for the calculated patterns were 5.8%, 4.3%, and 4.2%, respectively.

calculated using LCF based on V_2O_3 and V_2O_5 standards, which shows V(4.8+) for all materials.

2.2. Ion Transport and Structural Evolution upon Initial (Dis)charge

Substituting Zn^{2+} ions with Na^+ in the HYB electrolyte could affect ionic conductivity and therefore cycling behavior. To characterize ionic mobility within each electrolyte, the diffusion coefficients of h-NVO, NVO(300), and NVO(500) in the 1.0 M $ZnSO_4$ (ZS) and HYB electrolytes were evaluated using cyclic voltammetry, where the cathodes were first reduced from 1.4 V to 0.4 V versus Zn/Zn^{2+} and then oxidized from 0.4 V to 1.4 V versus Zn/Zn^{2+} , as shown in Figure 2. The Randles–Sevcik equation^[43,44] was used to describe the diffusion coefficient of a charged species. The peak current densities during the oxidation (≈ 0.6 V) and reduction (≈ 1.2 V) sweeps were evaluated using the Randles–Sevcik equation^[19,45–47] to determine the oxidation and reduction diffusion coefficients (Figure S3–S5, Supporting Information). As summarized in Table 1, higher diffusion coefficients were consistently observed during the oxidation process, along with decreased diffusion coefficients with increasing annealing

temperature of the parent NVO material. In h-NVO, higher diffusion coefficients were observed using the HYB electrolyte, while in NVO(300) systems, higher diffusion coefficients were observed using the ZS electrolyte. In the NVO(500) cells, diffusion coefficients were similar using both electrolytes. The diffusion coefficients calculated from the cyclic voltammetry experiments show that Na^+ incorporation in the HYB electrolyte does not negatively affect ionic mobility, and generally comparable diffusion coefficients using both the ZS and HYB electrolyte indicating that the HYB electrolyte are suitable for use in a Zn-ion battery.

2.3. Operando X-ray Powder Diffraction

Anhydrous NVO^[48] and monohydrated NVO^[49] structures have a similar electrochemical reduction mechanism, whereby after discharge in a Zn-aqueous battery, the insertion of Zn^{2+} and H^+ into NVO-based cathodes results in the formation of two new phases.^[18,19] The first phase, $Zn_4(SO_4)(OH)_6 \cdot 5H_2O$ [PDF# 00-039-0688], or zinc hydroxy-sulfate (ZHS), forms due to the small pH changes that accompany Zn^{2+}/H^+ insertion to the NVO lattice. The second phase, $Zn_3(OH)_2V_2O_7 \cdot 2H_2O$ [PDF# 00-50-570], or zinc

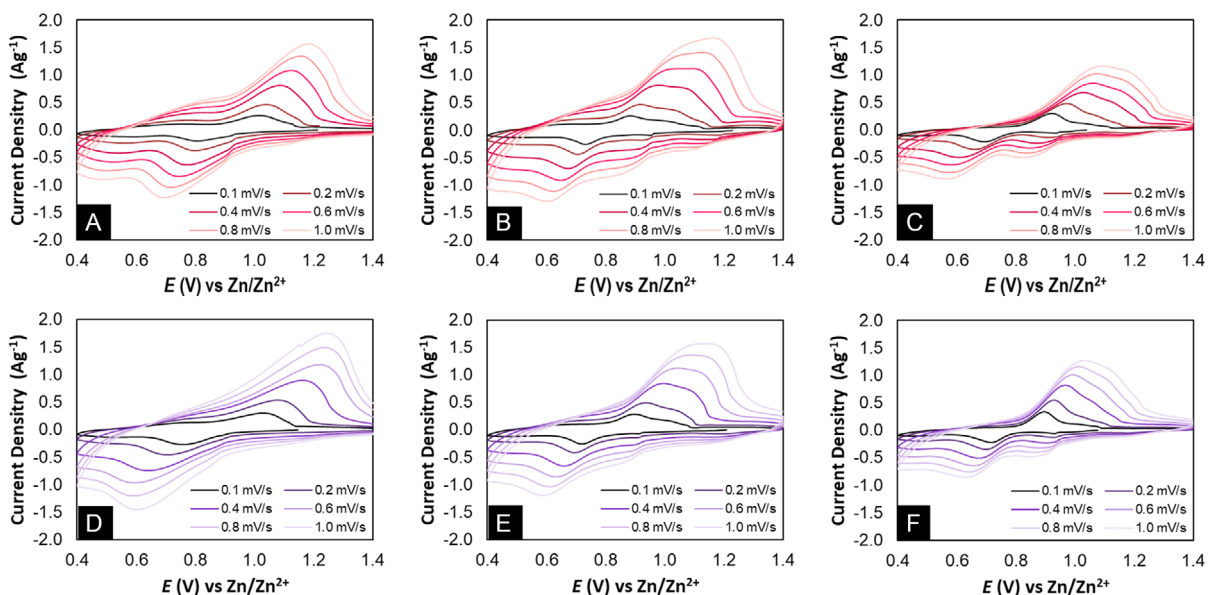


Figure 2. Cyclic voltammograms of A,D). h-NVO, B,E). NVO(300), and C,F). NVO(500) in ZS (red) (A–C), and HYB (purple) (D–F) electrolytes.

Table 1. Summary of diffusion coefficients determined using the Randles–Sevcik equation.

System	Slope (reduction) $[A \cdot (Vs)^{-\frac{1}{2}}]$	Diffusion Coefficient (reduction) $[cm^2 \cdot s^{-1}]$	Slope (oxidation) $[A \cdot (Vs)^{-\frac{1}{2}}]$	Diffusion Coefficient (oxidation) $[cm^2 \cdot s^{-1}]$
h-NVO_ZS	0.289	2.23 E-07	0.371	3.68 E-07
h-NVO_HYB	0.356	3.39 E-07	0.444	5.27 E-07
NVO(300)-ZS	0.283	2.14 E-07	0.392	4.11 E-07
NVO(300)-HYB	0.233	1.45 E-07	0.322	2.13 E-07
NVO(500)-ZS	0.197	1.04 E-07	0.253	1.71 E-07
NVO(500)-HYB	0.180	8.66 E-08	0.265	1.88 E-07

pyrovanadate (ZVO), forms upon Zn^{2+} insertion during discharge. Crystal structure diagrams of NVO, NVO \cdot H₂O, ZHS, and ZVO are provided in Figure S6, Supporting Information and tabular crystallographic parameters are in Table S2, Supporting Information. A prior spatially resolved *operando* XRD study indicates that the ZHS phase begins to form during discharge and is reversible upon charge.^[50] Unlike ZHS, ZVO formation occurs spontaneously at the separator-electrolyte interface after assembling the cell and progresses slowly (relative to ZHS) toward the current collector side during active discharge. Unlike ZHS formation, ZVO formation is only partially reversible upon charge, suggesting permanent Zn^{2+} insertion in the parent structure can lead to capacity fade from repeated cycling.

Figure 3 displays heatmaps generated from *operando* XRD experiments of NVO cells cycled at 100 mA·g⁻¹ between 0.4 and 1.4 V versus Zn/Zn²⁺ for one full cycle. Rietveld refinement was

performed for each pattern in the range of 0.7–2.5° 2θ and phase fractions of NVO, ZHS, and ZVO were calculated for each scan. The corresponding first cycle voltage profiles, dt/dV plots, and calculated phase fractions at each scan are presented alongside the XRD heatmap plots in Figure 3. The dt/dV plots are used similarly to traditional dq/dV plots where the peaks correspond to plateau regions in the voltage profiles. The differences between as a function of NVO type were evident based on the position of the (100) peak near 1.5° 2θ in the pristine state. In h-NVO, the peak was observed at a slightly lower angle, consistent with the refinements performed on the pristine electrodes. It should be noted that the relative positions of the NVO (100) and ZVO (001) peaks are different between h-NVO and NVO300/500, where the wider interplanar spacing of h-NVO causes the NVO (100) peak to be at lower angle than the ZVO (001) peak.

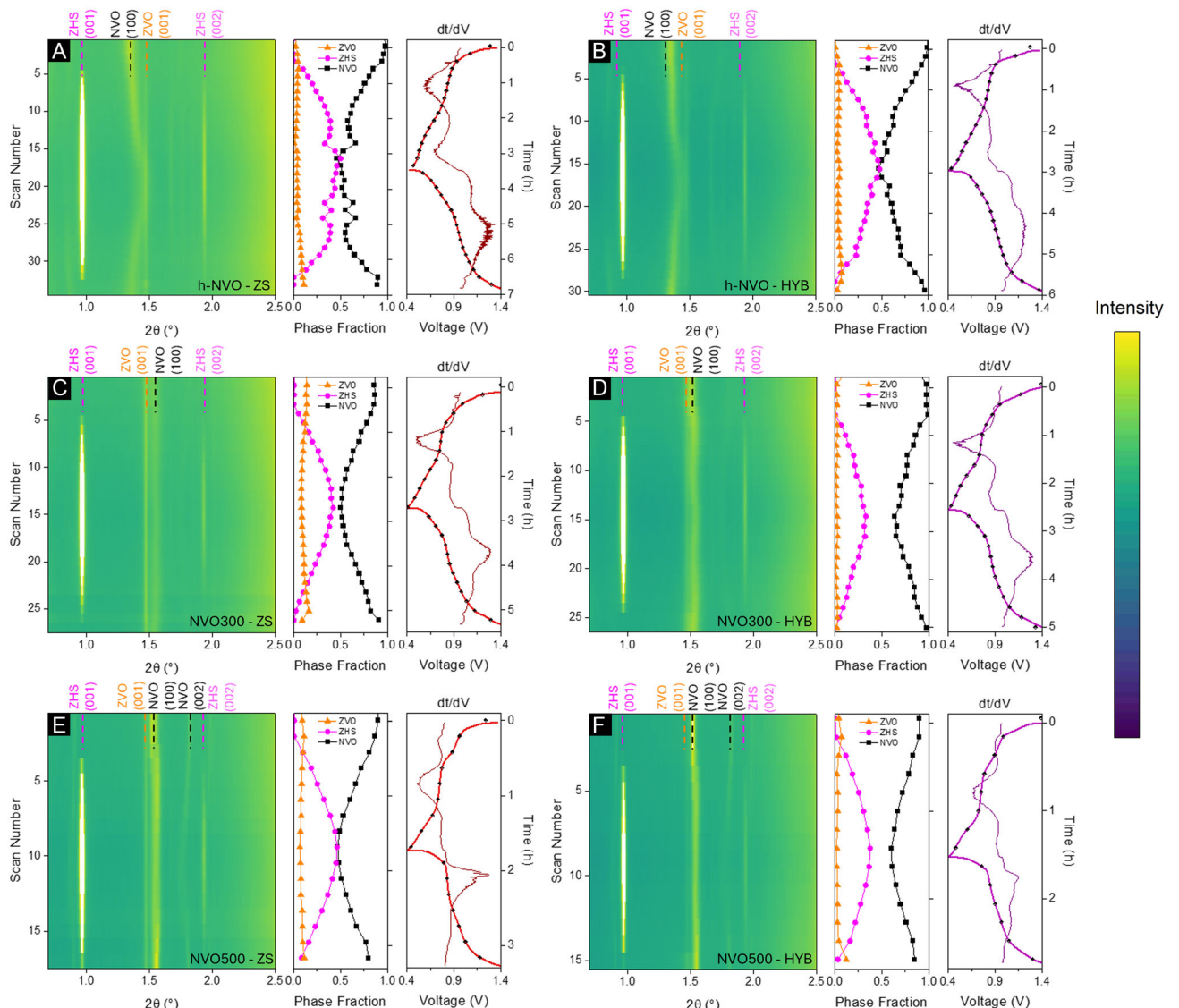


Figure 3. *Operando* XRD results of A,B) h-NVO, C,D) NVO300, and E,F) NVO500 in (A,C,E) ZS and (B,D,F) HYB electrolytes. The first cycle voltage profiles, first cycle dt/dV versus time plots, and phase fractions resulting from Rietveld refinement are plotted alongside each XRD heatmap. Select peaks corresponding to NVO, ZHS, and ZVO phases are highlighted in the XRD plots.

Upon cycling, the diffraction patterns provided insight into the (dis)charge mechanism within each NVO morphology. In h-NVO (Figure 3A,D), the intense NVO (100) peak shifted to a significantly higher angle, indicating a reduction in the (100) d-spacing. This was accompanied by significant ZHS formation, which reached a maximum phase fraction at the end of discharge. A small increase in ZVO phase fraction was also observed near the end of discharge, which coincided with a minor dt/dV peak and plateau in the voltage profile near ≈ 0.6 V. Similar phenomena were observed for both the ZS and HYB electrolytes, with the ZS electrolyte exhibiting a slightly higher capacity than the HYB electrolyte.

The diffraction patterns in the NVO300 (Figure 3B,E) and NVO500 (Figure 3C,F) cells displayed somewhat different behavior than those from the h-NVO cell. First, the NVO (100) peak shifted much less throughout (dis)charge in the NVO300 and NVO500 cells, as compared to the h-NVO cell. This was expected as the annealed materials exhibited lower capacity and, thus, less incorporation of new ions into the lattice. Second, in both cells using the ZS electrolyte, a significant ZVO peak (001) was observed, even in the pristine state. In contrast to the h-NVO cell, the intensity of the ZVO (001) peak in the NVO300/500 cells remained more consistent throughout the cycle, confirming its irreversibility, particularly compared to ZHS formation which was essentially fully reversible. This was further evidenced by the lack of a distinct ZVO formation peak in the dt/dV plots for NVO300 and NVO500.

In the NVO300 and NVO500 cells containing the HYB electrolyte, ZVO (001) intensity was significantly reduced in the pristine state and, again, did not change much during cycling. This observation was consistent with the hypothesis that the Na-containing HYB electrolyte stabilizes the NVO structure, mitigating spontaneous formation of irreversible ZVO and leading to enhanced capacity retention. In h-NVO, ZVO appeared to participate more reversibly, particularly in the HYB electrolyte. The structural water and wider interplanar spacing in h-NVO could lead to these mechanistic differences. Proton insertion (as H_3O^+) could be partially diminished since h-NVO already contained significant structural water and the wider channels could more easily facilitate reversible (de)insertion of Zn^{2+} ions in place of Na^+ . The reversible participation of Zn^{2+} leads to the improved capacity observed in h-NVO, as compared to NVO300 and NVO500.

Figure 4 further highlights the evolution of the NVO and ZVO phases throughout the first electrochemical cycle using a specific range between 1.25 and 1.65 $^\circ\text{2}\theta$. Representative peaks were identified and labeled for both ZVO and NVO, and the peak positions throughout cycling were tracked with dotted lines. The same dt/dV versus time plots from Figure 3 are plotted alongside the diffraction data to correlate electrochemical behavior and diffraction profiles phenomena. For each cell, a small amount of ZVO was present in the pristine state and throughout cycling. This was especially true for NVO300 and NVO500 in the ZS electrolyte (Figure 4B–C). The cells using the HYB electrolyte generally exhibited a less intense ZVO (001) peak throughout cycling than their ZS counterparts, and the cells with hydrated h-NVO typically exhibited a less intense ZVO peak than the cells with heat-treated

NVO300 and NVO500. These findings confirm that the heat-treated NVO materials (at 300 and 500 $^\circ\text{C}$) had a higher propensity for spontaneous Zn uptake to form ZVO, particularly when the Na_2SO_4 additive was not present in the electrolyte. Additionally, all three cell types displayed similar shifts in NVO (100) peak position and intensity throughout cycling, indicating shared electrochemical mechanisms. As protons and Zn^{2+} ions were inserted in the NVO structure during discharge, the NVO peak shifted to a higher 2θ (lower d-spacing) position and lost some intensity. The NVO peak subsequently shifted back to a lower 2θ position during charge and regained some intensity, with the largest shifts and intensity changes exhibited by the h-NVO cells, consistent with their enhanced capacity. These trends support the notion that the wide interlayer spacing of h-NVO facilitates high-capacity, reversible ion (de)insertion. Figure S7–S12, Supporting Information contain the XRD results plotted as typical intensity versus two theta plots as a function of scan number to further illustrate the processes discussed earlier.

To further explore the spontaneous formation of the ZVO phase, *ex situ* XRD patterns of recovered cathodes rested in coin cells for 168 h (1 week) and their respective pristine powders were collected. The OCV plots display a significant voltage drop in both the NVO300 and NVO500 materials in ZS electrolyte, while the samples treated in ZS/h-NVO remained relatively unchanged over the first few hours of rest (Figure 5A–C). The voltage drop in the heat-treated NVO300 and NVO500 materials is attributed to the fast loss of Na^+ from the NVO structure into the bulk electrolyte upon immersion of the cathode. The resulting VO layers are then stabilized by the spontaneous insertion of Zn^{2+} , forming an irreversible ZVO phase evidenced by the plateau that occurs around 1.25 V in the ZS systems. This effect is diminished in the ZS/h-NVO system, attributed to the contribution interlayer water plays in stabilizing the h-NVO layers (Figure 5A). *Ex situ* XRD of the 168 h rested cathodes displays a shift of the NVO (100) peak and the emergence of the ZVO (001) peak in the 5–20 $^\circ\text{2}\theta$ region (Figure 5D–F). The peak shift from the pristine powder to higher $^\circ\text{2}\theta$ in NVO300 and NVO500 indicates a decrease in interlayer spacing as a result of Zn^{2+} insertion into the NVO lattice, and the formation of a shoulder peak indicates the presence of the irreversible ZVO phase (Figure 5F–E). Qualitatively, the ZVO peak was more evident in the cathodes exposed to ZS electrolyte than those exposed to HYB electrolyte. The ZVO phase forms at a higher $^\circ\text{2}\theta$ in h-NVO since the hydrated state has greater interlayer spacing compared to NVO300 and NVO500 (Figure 5D). The magnitude of peak shift from the pristine powder between the ZS and HYB rested h-NVO, NVO300, and NVO500 cathodes was 0.5%, 2.0%, and 2.9%, respectively. A table of peak position and shift can be viewed in Table S11, Supporting Information. The OCV and XRD data confirm the spontaneous formation of ZVO and how its impact is reduced the greatest in the h-NVO system.

2.4. pH Determination

Electrolyte pH in aqueous batteries is important to analyze particularly when H^+ insertion can play a role in the redox

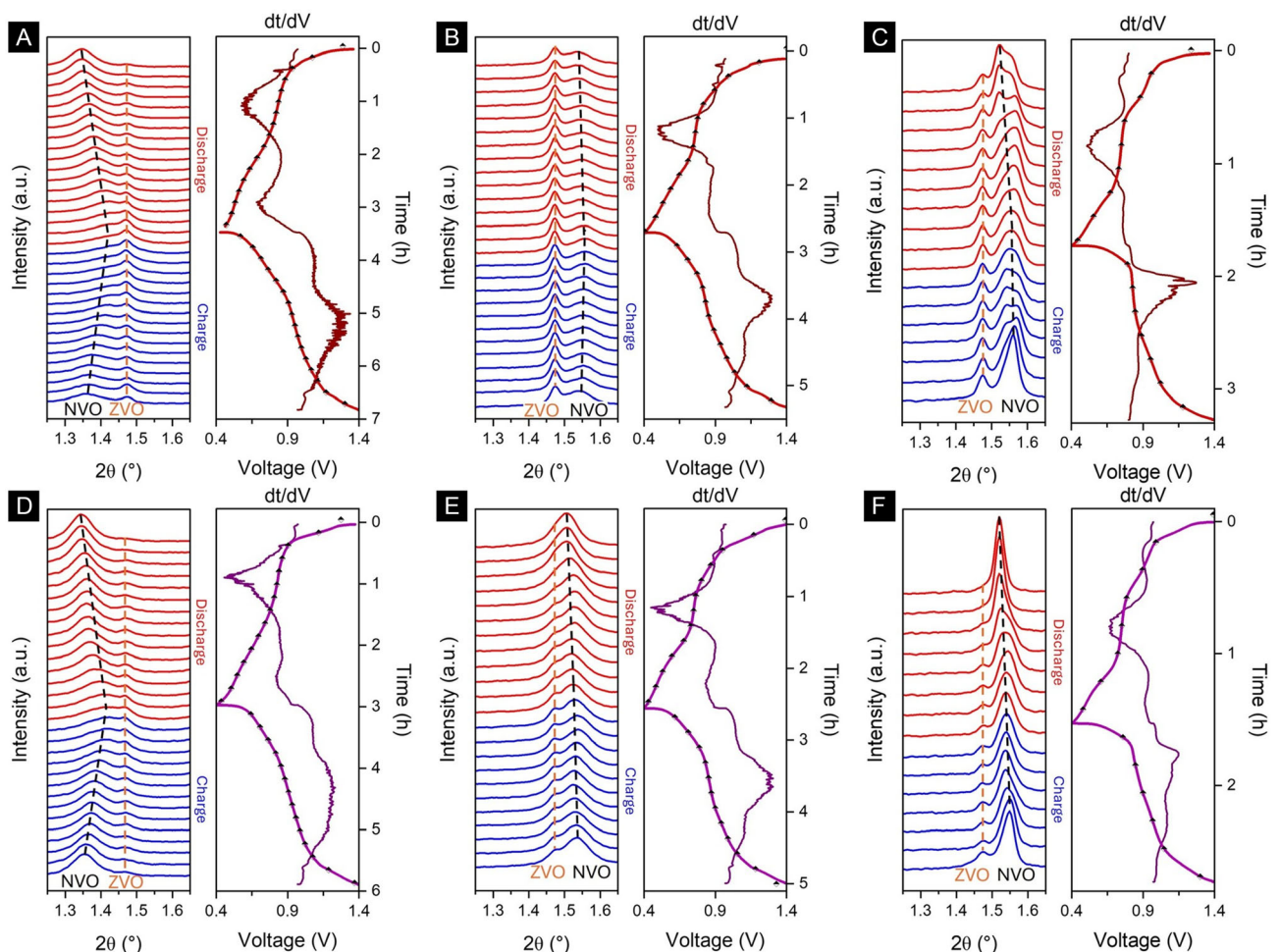


Figure 4. Operando XRD results of A,D) h-NVO, B,E) NVO300, and C,F) NVO500 in (A–C) ZS and (D–F) HYB electrolytes in the range of 1.25–1.65° θ . The first cycle voltage profiles and first cycle dt/dV versus time plots are plotted alongside each set of XRD data. Specific peaks for NVO and ZVO are labeled, and their peak positions are tracked by dotted lines.

mechanism.^[51–53] The pH values were measured before and after five cycles in the HYB and ZS electrolytes using specialized cells that contained pH electrodes. The initial pH of the ZS and HYB electrolytes exhibited similar pH values, as shown in Table 2. For this specific system, pH did not fluctuate substantially while cycling, unlike other Zn-aqueous systems that exhibit significant pH changes during cycling.^[54] Full overlayed pH and voltage versus time graphs are available in Figure S14, Supporting Information. Galvanostatic intermittent titration technique (GITT) was also performed in conjunction with pH measurements for h-NVO, NVO(300), and NVO(500) with the ZS and HYB aqueous electrolytes (Figure 6). The pH increase seen during the first pulse and relaxation suggests proton insertion into the cathode immediately following application of current; however, the pH of each system begins to stabilize over the duration of the first discharge and remains consistent during charge. It would be expected for the pH to increase as proton insertion occurs due to remaining OH⁻; however, pH was not significantly impacted beyond the first GITT pulse. It is likely that the expected pH changes are moderated by the formation of ZHS. During the pulse windows, plateaus are visible in the pH data. These plateaus are the result

of a change in the electric field and resulting ion concentration from the current pulse. The HYB cells produced smaller pH plateaus than ZS cells, which could be attributed to a difference in ion density due to the presence of Na⁺ ion in addition to Zn²⁺.

2.5. Electrochemical Behavior upon Extended (Dis)charge Cycling

The (dis)charge behavior of the three NVO materials with ZS and HYB electrolytes was evaluated through long-term galvanostatic cycling. As shown in Figure 7, the decrease in charge and discharge capacities from cycle 1 to 15 is greater than the decrease in capacities from cycle 15 to 30 across all systems, indicating that the capacity fade slows down as the active material stabilizes following repeated Zn²⁺ and H⁺ (de)insertion.

In the extended cycling results shown in Figure 8, and summarized in Table S3–S8, Supporting Information, lower specific capacities were observed with increasing annealing temperature of the parent NVO material. Furthermore, lower capacities were observed when using the Na-incorporated HYB electrolyte across all three NVO materials.

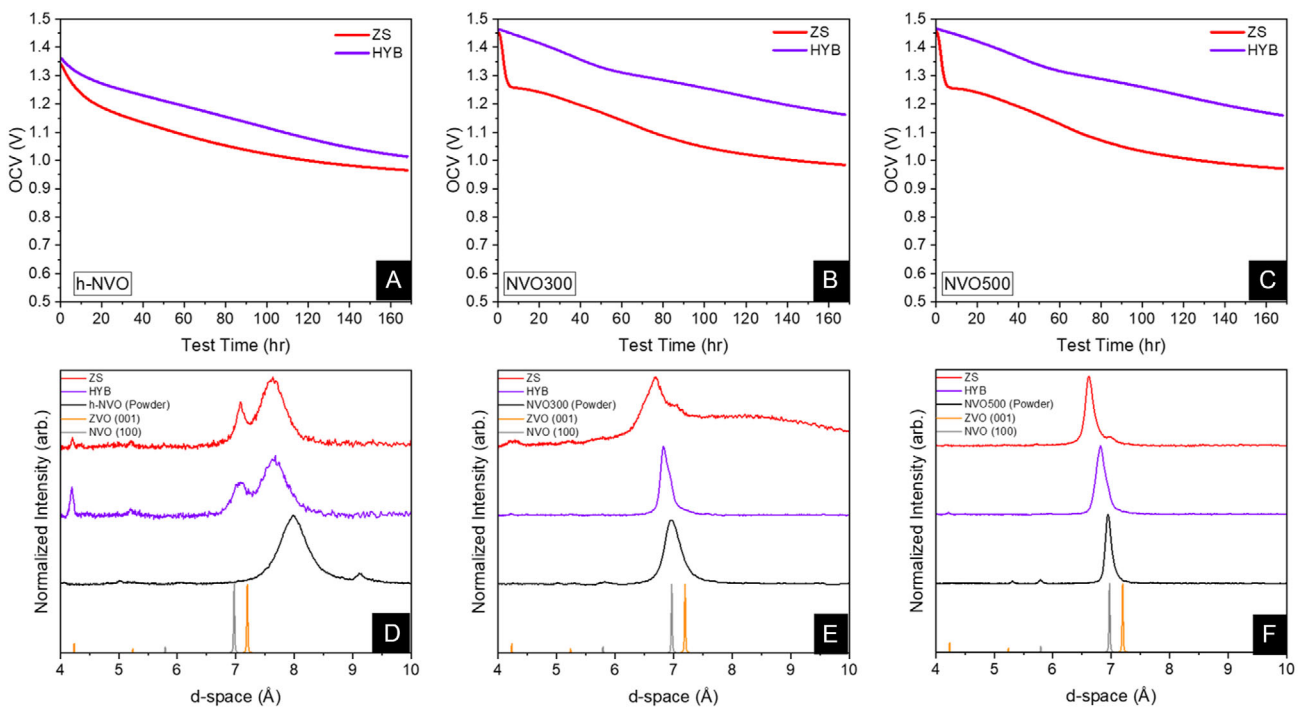


Figure 5. A–C) Open circuit voltage versus time after rest for HYB (purple) and ZS (red) electrolyte containing zinc coin cells with h-NVO (A), NVO300 (B), and NVO500 (C) cathodes. D–F) *Ex situ* XRD patterns plotted in d-space of the recovered h-NVO (D), NVO300 (E) and NVO500 (F) cathodes from cells with ZS (red) and HYB (purple) electrolytes with their respective pristine and CIF reference powder diffraction patterns. Pristine powders in black, ZVO in orange, and NVO in gray.

Table 2. Summary of *operando* pH data from Zn/NVO cells containing differing NVO materials and electrolytes measured before cycling and after the first and fifth charge cycle.

Material (Electrolyte)	Initial pH	pH 1st Cycle Charge	pH 5th Cycle Charge	pH 1st Cycle Discharge	pH 5th Cycle Discharge
h-NVO-ZS	5.65	5.58	5.56	5.74	5.65
h-NVO-HYB	5.66	5.91	5.78	5.78	5.76
NVO300-ZS	5.68	5.73	5.70	5.60	5.66
NVO300-HYB	5.25	5.89	5.74	5.78	5.92
NVO500-ZS	5.75	5.86	5.82	5.82	5.77
NVO500-HYB	5.86	5.91	5.92	5.99	6.02

However, when using the HYB electrolyte, the rate of capacity fade was lower. To account for the early capacity fade rate changes due to Zn^{2+} and H^+ stabilization, the percentage capacity fade for each cell was calculated by dividing the highest achieved specific capacity by the specific capacity of the last cycle. Using an h-NVO cathode with ZS electrolyte, the specific capacity decreased by 24% from the greatest discharge capacity after 120 cycles and 4% with the HYB electrolyte. In cells with the NVO(300) cathode and ZS electrolyte, the specific capacity decreased by 19% after 120 cycles and 2% when using the HYB electrolyte. In NVO(500), which had a significantly lower functional capacity under these conditions, the specific capacity using the ZS electrolyte decreased by 44% after 120 cycles, which was limited to 39% when using the HYB electrolyte. Across all three materials, it is clear that with the incorporation of Na_2SO_4 into the electrolyte, there is a tradeoff between

improved capacity retention with lower specific capacity. A “delayed” cycling study was conducted after resting assembled coin cells for 168 h (1 week) in ZS and HYB electrolytes to determine the HYB and ZS electrolytes’ impact on the degradation of the active material. The h-NVO morphology, yielding the lowest capacity fade of the three morphologies assessed in Figure 7, 8, was selected for the cycling study (Figure 7G,H). While overall delivered capacity decreased in both the delayed ZS and HYB cells compared to the non-delayed cells, capacity faded only 5% in the delayed HYB electrolyte, while a significant 45% fade was observed in the delayed ZS cell. The rate of fade of capacity fade in the HYB remained robust after the delay time while the delayed ZS cell exhibited a significantly increased rate of fade. This study indicates that the HYB electrolyte is effective at inhibiting the degradation of the cathode material in the absence of current load.

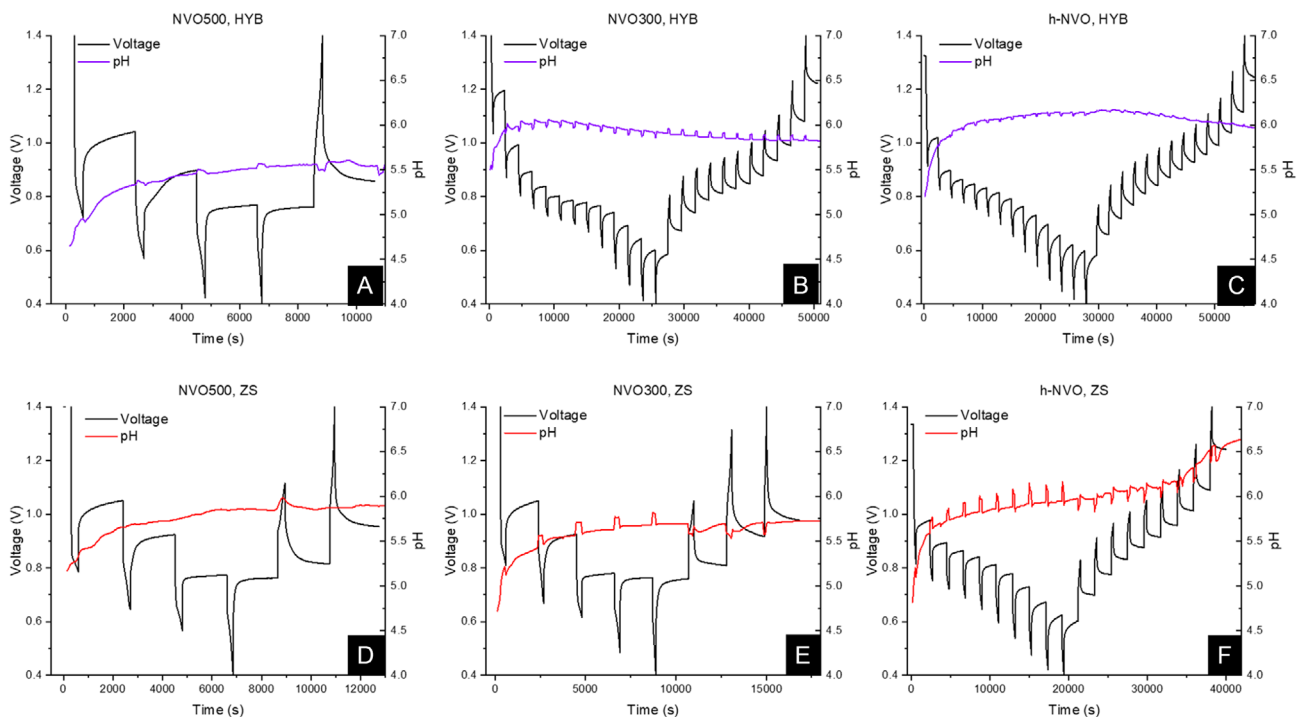


Figure 6. Galvanostatic intermittent titration technique (GITT) was performed in conjunction with pH electrode measurements for h-NVO C,F), NVO(300 B,E), and NVO(500) A,D) with the ZS (red) (D-F) and HYB (purple) (A-C) aqueous electrolytes.

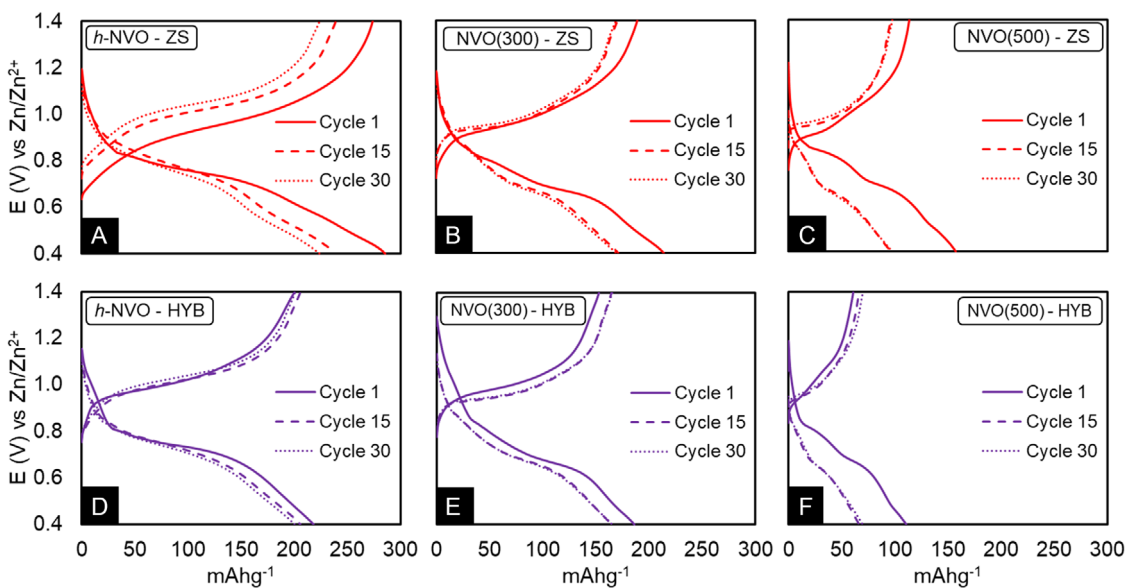


Figure 7. Voltage profiles of select (dis)charge cycles of Zn/NVO cells with A,D). h-NVO, B,E). NVO(300), and C,F). NVO(500) cathodes with ZS (red) (A–C) and HYB (purple) (D–F) electrolytes.

2.6. Post-Cycling Deposition Analysis

The deposition of electrolyte solvated transition metal species that originate from the positive electrode and deposit on the negative electrode, known as cross-talk, has been noted to be responsible for premature cell failure in Li-ion batteries.^[55,56] X-Ray spectroscopy-based imaging probes can be valuable to

determine heterogeneity at the mesoscale.^[57] Herein, cells with NVO-positive electrodes and Zn-negative electrodes were cycled at 1000 mA·g⁻¹ for 30 cycles between 1.4 and 0.4 V versus Zn/Zn²⁺. Following cell disassembly, X-ray fluorescence maps (Figure 9) of V K-edge on the Zn electrodes were taken. These maps provide evidence of V dissolution from the cathode and its subsequent deposition on the Zn anode in the h-NVO and

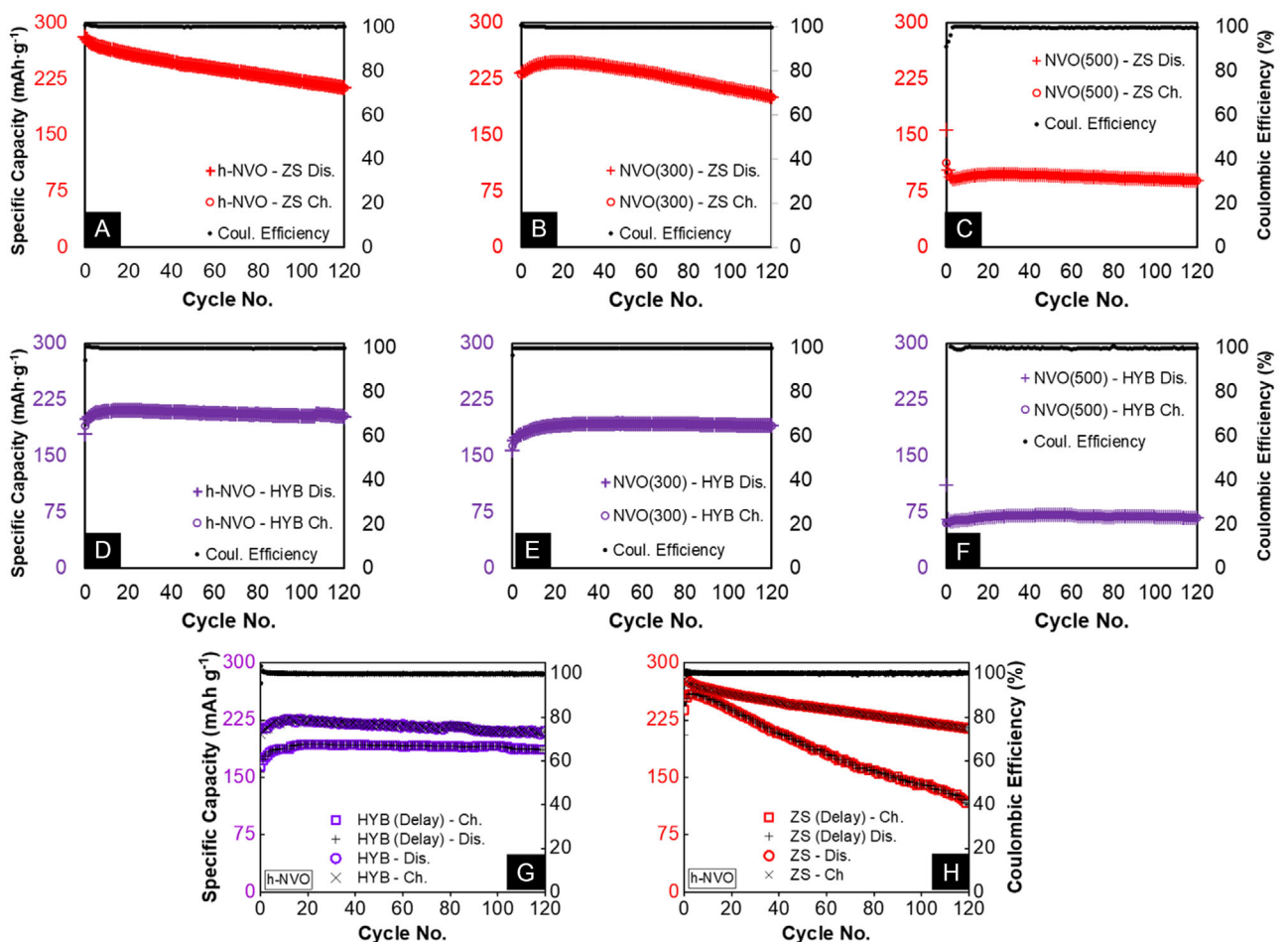


Figure 8. Galvanostatic cycling from 0.4 to 1.4 V at 1000 mA g⁻¹ of cells with A,D) h-NVO, B,E) NVO(300), and C,F) NVO(500) cathodes in ZS (red) (A–C), and HYB (purple) (D–F) electrolytes. Cycling test with and without a 168 h delay of cells with h-NVO cathodes G,H) in ZS (red) (H), and HYB (purple) (G) electrolytes.

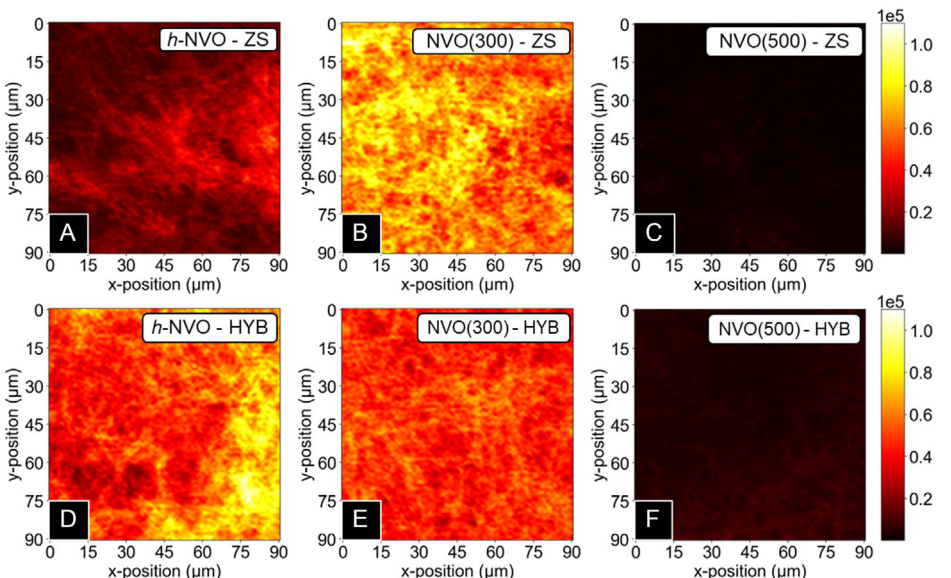


Figure 9. X-ray fluorescence maps of V K-edge on Zn anodes recovered from cells containing h-NVO, A,D) NVO300, B,E) and NVO500, C,F) cathodes with ZS (A–C) and HYB (D–F) electrolytes cycled at 1.0 A g⁻¹ for 30 cycles between 1.4 V and 0.4 V versus Zn/Zn²⁺.

NVO(300) systems, but not in the NVO(500) system. These findings are attributed to the larger crystallite size of the NVO(500) parent material and lower functional capacity of the Zn/NVO(500) cells under this test condition (Figure 8), both decreasing the amount of V dissolution from the positive electrode relative to the h-NVO and NVO(300) counterparts.

2.7. Dissolution Study

Following an approach previously developed for investigation of vanadium oxides and phosphates in lithium-based nonaqueous electrolytes,^[58] a study was conducted herein to measure the dissolution kinetics of V and Na from h-NVO, NVO(300), and NVO(500) when immersed in the ZS and HYB aqueous electrolytes (Figure 10). Pristine electrodes were sealed in a pouch and immersed in the electrolyte solution. Discharged and charged electrodes were first cycled at 100 mA g⁻¹ and

recovered from cells before being sealed and immersed in an electrolyte solution. In order to unambiguously relate the observations to the properties of the NVO material and the electrolyte composition rather than differences in state of (dis)charge, a capacity limit of 200 mAh·g⁻¹ was used for this test. The electrolyte was periodically sampled, and ICP-OES analysis was conducted to measure V concentrations in the electrolyte. The time-resolved V concentration profiles were analyzed by (Equation 1), the Noyes–Whitney equation,^[59] which is used to describe dissolution of solid particles into liquids

$$\frac{dC}{dt} = k(C_s - C) \quad (1)$$

In (Equation 1), C represents the measured concentration at time t , k represents the rate constant, and C_s is the equilibrium concentration. Upon integration with respect to t , (Equation 2) is obtained

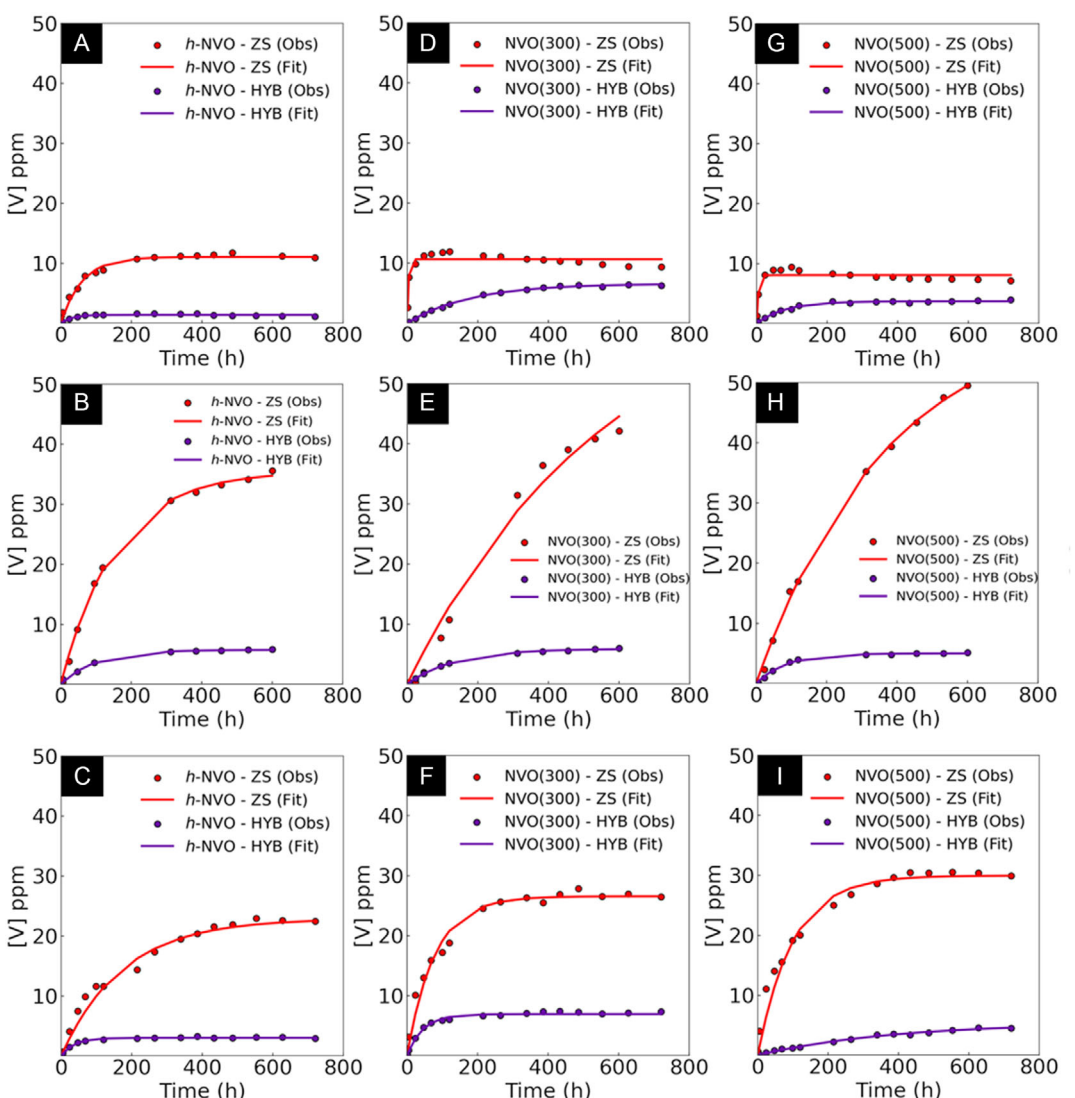


Figure 10. Observed and calculated V dissolution profiles of A,B,C) h-NVO, D,E,F) NVO(300), and G,H,I) NVO(500) cathodes in ZS (red) and HYB (purple) electrolytes in the (A,D,G) pristine, (B,E,H) discharged, and (C,F,I) charged states.

$$C = C_s(1 - e^{-kt}) \quad (2)$$

From (Equation 2), the extent of dissolution is dependent on the time elapsed since electrolyte immersion (t), the equilibrium solubility of the species, and a constant, k , which describes the rate of dissolution. Since C_s and C are directly proportional, determining the equilibrium concentration can provide a comparative basis for h-NVO, NVO(300), and NVO(500) in ZS and HYB electrolytes in the pristine, discharged, and charged states.

The Noyes–Whitney model also assumes the existence of a thin diffusion layer^[60] between the NVO electrode and the electrolyte; transport of solvated molecules through this diffusion layer is the rate limiting step.

Table 3 summarizes and Table S9, Supporting Information details the observed and calculated V dissolution profiles of h-NVO, NVO(300), and NVO(500) cathodes in ZS and HYB electrolytes in the pristine, discharged, and charged states. The data indicate that the equilibrium V concentration (V_{Cs}) with pristine h-NVO was $\approx 10X$ lower when immersed in HYB electrolyte relative to the ZS electrolyte. With discharged h-NVO electrodes, the $V_{Cs} \approx 6X$ lower in the HYB electrolyte relative to the ZS electrolyte while after charge, the V_{Cs} of h-NVO electrodes were $\approx 7X$ lower in the HYB than in the ZS electrolyte. For pristine NVO(300) and NVO(500) electrodes, the impact of electrolyte was less pronounced for the pristine material; however, after discharge, there was a $\approx 10X$ lower solubility for both materials in the HYB electrolyte relative to the ZS electrolyte, with $\approx 3X$ lower solubility for NVO(300) and $\approx 5X$ lower solubility for NVO(500) in the HYB electrolyte relative to the ZS electrolyte.

There are two key findings in the V dissolution profiles: First, the incorporation of Na in the electrolyte leads to a decrease in V dissolution, as seen by the lower V_{Cs} observed in h-NVO, NVO(300), and NVO(500) electrodes when immersed in the HYB electrolyte. Second, V_{Cs} is lowest in the pristine materials and generally highest in the discharged materials. Using the HYB electrolyte, which contains added Na, effectively limits V dissolution even during active electrochemical cycling. This is consistent with the slower rate of capacity fade observed during electrochemical testing (Figure 8) when using the HYB electrolyte.

The equilibrium concentration of sodium, or Na_{Cs} , in the ZS electrolyte was measured for h-NVO, NVO(300), and NVO(500) in both their pristine and charged states. As summarized in Figure S13 and Table S10, Supporting Information, nearly all

the Na from the parent electrodes dissolves into the electrolyte upon immersion.

2.8. Operando X-ray Absorption Spectroscopy

XAS provides valuable information about local coordination environment in vanadium systems.^[61] *Operando* XAS was used to study the effect of NVO and electrolyte type on the vanadium oxidation state of NVO samples in a functional aqueous Zn battery. XAS measurements were collected during a full discharge/charge cycle at a current density of 100 mA g⁻¹ between 1.4 and 0.4 V versus Zn/Zn²⁺ in ZS and HYB electrolytes.

The *operando* XAS at XANES region of V K-edge in NVO cells during discharge (Figure 11A–F) and charge (Figure S15, Supporting Information), using reference data derived from the literature.^[62] Both edge positions shift to lower energy during discharge and shift to higher energy during charge for NVO cells, but the edge position of h-NVO shifted most, followed by NVO(300) and then NVO(500) cells. The oxidation states of vanadium following discharge and charge in ZS and HYB electrolytes are provided in Table 4. The V oxidation states in pristine *operando* cells are lower than the as-synthesized powders in the ZS electrolytes due to spontaneous formation of Zn₃(OH)₂V₂O₇·2H₂O(ZVO) as V centers are reduced to accommodate the inserted Zn²⁺ ions, as described in *operando* XRD results (Figure 3). The V oxidation states with the HYB electrolyte in pristine cells are similar to the pristine powder due to the spontaneous ZVO formation is minimized by using the HYB electrolyte. The V oxidation states changed more during (dis)charge in cells ZS electrolytes than the cells in HYB electrolytes for h-NVO and NVO(300). The V oxidation states changes are similar for NVO(500) in the cells for both electrolytes. This is consistent with the electrochemistry (Figure 7), where h-NVO and NVO(300) in ZS electrolyte showed higher capacity than the cell in HYB electrolyte, but the capacity is similar for NVO(500) in both electrolytes.

The *operando* XANES data in Figure 11A–F and S14, Supporting Information show a pre-edge feature preceding the V K-edge during discharge and charge. The evaluation of the pre-edge feature provides insights for the evaluation of symmetries: tetrahedral (T_d), octahedral (O_h), and the square pyramidal (P_y) coordination of V⁵⁺, V⁴⁺, and V³⁺, where V³⁺ has O_h symmetry, V⁴⁺ has O_h and P_y coordinations, and V⁵⁺ has all three

Table 3. Dissolution summary for h-NVO, NVO(300), and NVO(500) materials in ZS and HYB electrolytes in the pristine, discharged, and charged states.

Material/Electrolyte	Pristine		Discharged		Charged	
	C _s (ppm)	k	C _s (ppm)	k	C _s (ppm)	k
h-NVO-ZS	11.1	0.0168	35.4	0.0064	22.9	0.0057
h-NVO-HYB	1.4	0.0338	5.7	0.0103	3.0	0.2969
NVO(300)-ZS	10.6	0.2955	68.4	0.0018	26.5	0.0127
NVO(300)-HYB	6.5	0.0056	5.9	0.0074	6.9	0.0223
NVO(500)-ZS	8.1	0.2124	61.7	0.0027	29.9	0.0101
NVO(500)-HYB	3.7	0.0125	5.0	0.0119	5.4	0.0026

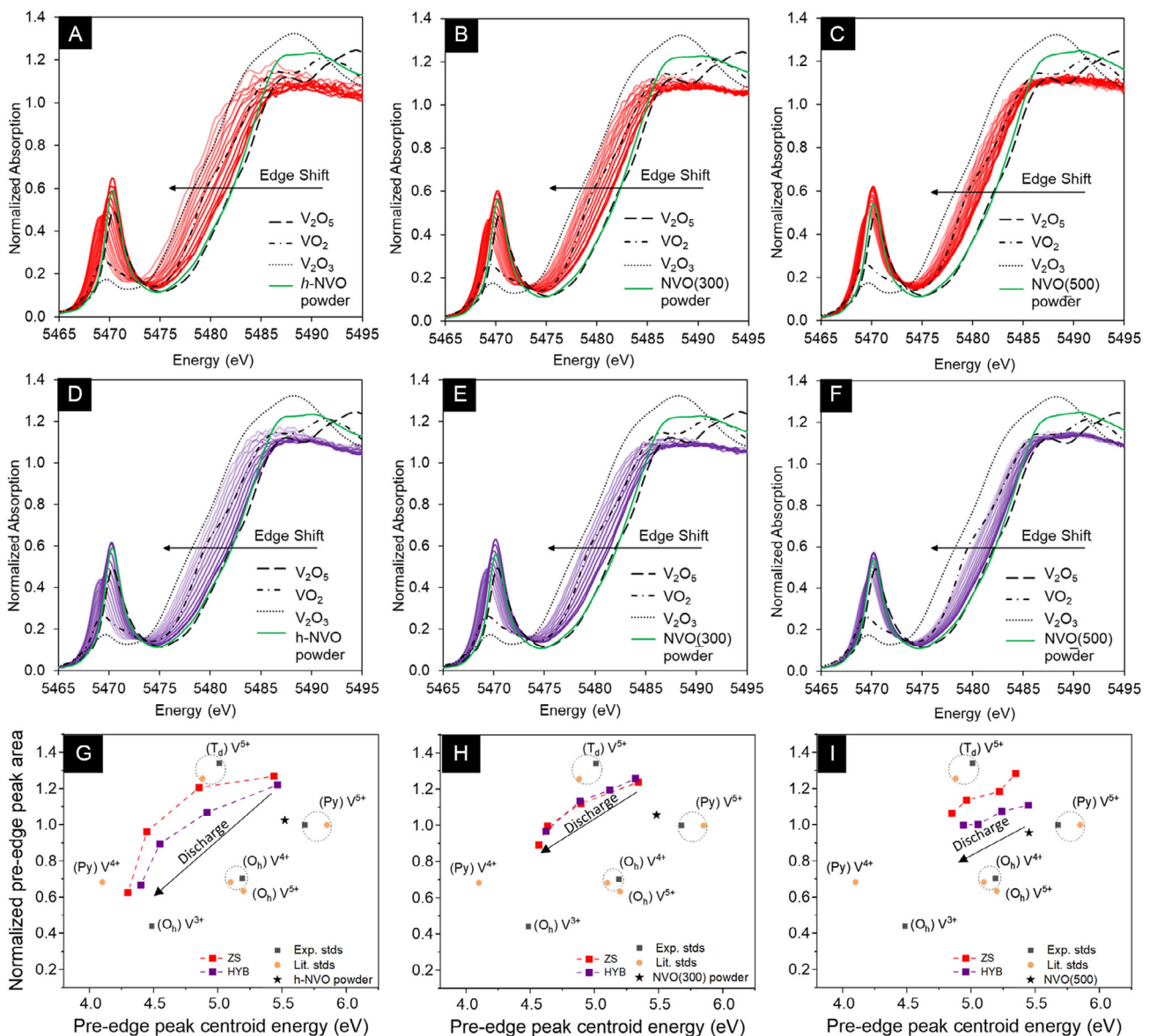


Figure 11. A–F Operando X-ray absorption spectra of V K-edge NVO cells during discharge in (A–C) ZS and (D–F) HYB electrolytes of (A,D) h-NVO; (B,E) NVO(300); and (C,F) NVO(500). G–I) The pre-edge feature of the correlations between normalized pre-edge peak area and its centroid position for the symmetry information of (G) h-NVO; (H) NVO(300); and (I) NVO(500) with selected scans during discharge.

		h-NVO	NVO(300)	NVO(500)
ZS	Pristine cell	4.73	4.62	4.44
	End of discharge	3.00	3.38	3.50
	End of charge	4.79	4.70	4.14
HYB	Pristine cell	4.93	4.66	4.89
	End of discharge	3.44	3.47	3.96
	End of charge	4.94	4.84	4.51

symmetries.^[63] The pre-edge peak's position and area have been linked to the oxidation state and coordination environment of V, respectively. The pre-edge feature of the correlations between

normalized pre-edge peak area and its centroid position to determine the symmetry information for vanadium based on the methodology developed by Chaurand et al.^[62] The XAS of $NaVO_3$, V_2O_5 , V_2O_4 , and V_2O_3 standards were collected for $V^{5+}(T_d)$, $V^{5+}(Py)$, $V^{4+}(O_h)$, and $V^{3+}(O_h)$. The standards reported from literature^[62] were extracted and normalized against $(Py)V^{5+}$ for comparison.

In an octahedral (O_h) environment, the presence of an inversion center prevents electronic transitions from the 1s core level to the empty 3 d levels, which results in a minimized pre-edge feature intensity. However, distortion in the $VO_6 O_h$ environment, such as in a pyramidal (Py) VO_5 or tetrahedral (T_d) VO_4 , leads to the loss of the inversion center and mixing of the 3 d orbital with the 4p orbital, which causes an increased pre-edge feature intensity

due to electron density being allowed in the 3d orbitals.^[64] Figure 11G–I shows distorted V O_h and P_y centers, which explains the presence of pre-edge features in NVO XAS spectra.

The pre-edge peak was analyzed for as-synthesized h-NVO, NVO(300), and NVO(500). The local environment for V appears to be similar for all three NVO materials and associated with V⁵⁺ asymmetric square pyramidal geometry (Figure S2, Supporting Information). In Figure 11G–I, all three NVO materials display a shift toward a T_d environment (increased peak area) when incorporated into *operando* cells. This is attributed to the spontaneous formation of ZVO from ion exchange prior to discharge as shown in Figure 3, consistent with VO₄-type tetrahedra coordination environment of V as shown in Figure S6d, Supporting Information. The contribution of the T_d environment to the pre-edge is larger for the NVO cells with the ZS electrolyte than the cell with HYB electrolyte. This is consistent with the lower V oxidation states for h-NVO and NVO(500) cells using ZS electrolyte prior to active discharge (Figure S15, Supporting Information and Table 4), as V centers are reduced to accommodate the inserted Zn²⁺ ions. This is also consistent with the *operando* XRD results that indicated less ZVO spontaneously formed at the pristine state when using HYB electrolyte.

The pre-edge peak position and intensity decreases during discharge and increases during charge, which indicates the symmetric environment of materials is reversibly changing. In the case of h-NVO, the pre-edge features starting from the middle of T_d and P_y of V⁵⁺ progress toward O_h environments (V³⁺) and P_y environments (V⁴⁺) during discharge as increased Zn²⁺ exchange with Na⁺ in the NVO structure is allowed due to the increased solubility of Na⁺ in the electrolyte. The V coordination environment is close to T_d (V⁵⁺) in ZS electrolytes while closer to P_y (V⁵⁺) in HYB electrolytes during discharge. In the case of NVO(300), the V coordination environments in both electrolytes are very similar that starting. Earlier, it was assessed from the XRD and TGA data that the annealing up to 300 °C results in loss of structural water, with no significant increase in crystallite size. Since solvation of Zn²⁺ ions is likely conducive to ion mobility due to a decrease in cation–cation repulsion, the loss of structural water may limit ion mobility in NVO(300) materials, whereas the extent of Na⁺-Zn²⁺ exchange may be more rate limiting in h-NVO and NVO(300). In the case of NVO(500), the pristine state V coordination environments is closer to T_d (V⁵⁺) in ZS electrolytes while closer to P_y (V⁵⁺) in HYB electrolytes, toward P_y V⁴⁺. The discharged h-NVO cells show a V environment more O_h in character (V³⁺) when compared with NVO(300) and NVO(500) consistent with the *operando* XRD results that more ZVO appeared to participate in the electrochemical reduction process, particularly in the HYB electrolyte.

3. Conclusion

Three NVO materials, h-NVO [Na_{1.15}V₃O·1.65H₂O], NVO(300) [Na_{1.13}V₃O₈·0.44H₂O], and NVO(500) [Na_{1.15}V₃O·0.14H₂O], were synthesized by annealing under air and electrochemically interrogated in two electrolytes: ZS (1.0 M ZnSO₄) and HYB (0.5 M

ZnSO₄ + 0.5 M Na₂SO₄). Cyclic voltammetry demonstrated comparable diffusion coefficients in both electrolytes, and long-term cycling revealed slower capacity fade but reduced capacity using the HYB electrolyte. Using ICP-OES, dissolution profiles of V and Na were determined, and it was found that Na-incorporated HYB electrolyte was effective in suppressing V dissolution throughout electrochemical cycling. *Operando* XAS was used to track changes in the V oxidation state in NVO pouch cells, revealing reduced reduction of V centers and, therefore, reduced capacity, in cells with the HYB electrolyte. Analysis of pre-edge features of V K-edge absorption spectra revealed that upon cell assembly, the V coordination is less tetrahedral in cells with the HYB electrolyte, suggesting reduced Na⁺-Zn²⁺ exchange (and thus less ZVO formation) due to the lower solubility of Na⁺ in the HYB electrolyte. *Operando* diffraction measurements confirmed the irreversible formation ZVO in cells using the ZS electrolyte, while the HYB electrolyte suppressed irreversible ZVO formation, attributed to the addition of Na⁺ in the HYB electrolyte which may inhibit the dissolution/ion-exchange of Na⁺ and Zn²⁺. Suppression of cathode dissolution in aqueous electrolytes while preserving the cost-effectiveness, safety, and scalability of aqueous Zn-ion batteries is critical for future adoption in grid-scale applications. The benefits of a facile electrolyte-additive method were illustrated here, with progress towards mechanistic understanding.

4. Experimental Section

Material Synthesis and Characterization

Hydrated NaV₃O₈, or h-NVO, was synthesized using a method adopted from previous studies.^[18,19] Briefly, V₂O₅ was suspended in an aqueous, N₂-degassed NaOH solution at 50 °C for 24 h. h-NVO was annealed in air at 300 °C to form NVO(300) and at 500 °C to form NVO(500). Water content of h-NVO, NVO(300), and NVO(500) powders was determined using a Thermal Analysis Q500 thermogravimetric analysis (TGA) instrument. XPD patterns of the NVO cathodes were collected using the 28-ID-1 XPD (PDF) beamline at the National Synchrotron Light Source-II (NSLS-II) facility in Brookhaven National Lab, followed by Rietveld refinement^[65,66] of the patterns using the GSAS-II and Profex software suites^[67] to determine crystal structure parameters. The stoichiometric ratio of Na:V in h-NVO, NVO(300), and NVO(500) was determined by first dissolving the samples in 5% HNO₃ and collecting the Na and V optical emission intensities using a Thermo Scientific iCAP 7000 Series ICP-OES instrument. The optical emission wavelengths selected for Na and V intensities were 589.5 nm and 309.3 nm, respectively.

Electrochemistry

Self-supporting 3D NVO-based electrodes were fabricated by incorporating h-NVO, NVO(300), or NVO(500) powders with conductive multiwall carbon nanotubes (MWCNTs) in a 7:3 mass ratio of NVO:MWCNTs. Two electrolyte compositions were prepared by dissolving their respective salts in deionized water. One electrolyte composition was 1.0 M ZnSO₄ (ZS) and the other was 0.5 M ZnSO₄ + 0.5 M Na₂SO₄ (HYB).

Coin-type cells were assembled for electrochemical testing using a Zn-foil anode, glass-fiber separator, NVO cathode, and either ZS or

HYB electrolyte. A BioLogic VSP potentiostat was used for cyclic voltammetry analysis, and a MACCOR battery tester was used for the galvanostatic cycling analysis.

Dissolution Studies

Dissolution analysis of h-NVO, NVO(300), and NVO(500) in ZS and HYB electrolytes was performed using the NVO:MWCNT electrodes described earlier. Charged and discharged cathodes used in the dissolution analysis were prepared by cycling to the desired state in a coin-cell and recovered by disassembling the cell. The electrodes were sealed in hydrophilic polypropylene pouches. The pouch-sealed electrodes were immersed in 25 mL of electrolyte, and aliquots of 0.8 mL of the electrolyte were periodically collected. The setup was perturbed at 200 rpm on a shaker table to maintain electrolyte homogeneity. The collected aliquots were diluted with 5% nitric acid, and optical emission spectra of V and Na were collected using a Thermo Scientific iCAP 7000 Series ICP-OES. Fitting was performed using a nonlinear regression model to minimize the sum of least-squares by varying the C_s and k parameters for the Noyes-Whitney equation.^[59]

Post-Electrochemical Characterization

Zn anodes were recovered from disassembled coin cells following cycling. Cells were in a charged state when disassembled. Recovered Zn anodes were sealed inside polyimide film. X-ray fluorescence mapping measurements were collected at the 5-ID submicron resolution X-ray spectroscopy (SRX) beamline at NSLS-II. 90 $\mu\text{m} \times 90 \mu\text{m}$ maps were collected at 6.0 keV. V contribution to the fluorescence intensity was fit using the PyXRF software suite.^[68]

Pouch-type cells were assembled for *operando* measurements using Zn anodes, glass-fiber separators, NVO cathodes, and Ni-tab current collectors. X-ray diffraction (XRD) measurements were done in the Debye-Scherrer configuration. XRD patterns were collected at the 28-ID-1 (PDF) beamline at NSLS-II. A powdered sample of NIST Standard Reference Material 660 lanthanum hexaborate (LaB_6) was used to calibrate the beamline to 0.1847 Å.

Transmission mode *operando* X-ray absorption measurements were collected using pouch-type cells. h-NVO, NVO(300), NVO(500), V_2O_5 , VO_2 , V_2O_3 , and VO reference samples were prepared by incorporation into boron nitride pellets. Measurements were collected at the 7-BM Quick Absorption Spectroscopy (QAS) beamline at NSLS-II. Athena software from the Demeter package^[69,70] was used to analyze the vanadium oxidation states by linear combination fitting (LCF). The edge energy for *operando* cells was selected at 0.6 normalized absorption intensity. The pre-edge feature was analyzed from the XANES data using a methodology developed by Chaur and et al.^[62] where pre-edge peaks were obtained by subtracting the background using a spline function and were fit with 2-3 Voigt peaks. V_2O_5 (V^{5+}), VO_2 (V^{4+}), V_2O_3 (V^{3+}), and VO (V^{2+}) standards were used to interpolate the oxidation states of V in the *operando* XAS cell scans. All peak areas were normalized to the V_2O_5 standard.

Acknowledgements

A.N., G.S. and R.C. H. Co-first authors and contributed equally. The mechanistic studies were supported as part of the Center for Mesoscale Transport Properties, an Energy Frontier Research Center supported by the U.S. Department of Energy Office of

Science under Award #DE-SC0012673. Electrochemical testing to understand battery resilience under extended cycling (Figure 8) relates to Department of Navy award N00014-20-1-2858 issued by the Office of Naval Research (ONR). The United States Government has a royalty-free license throughout the world in all copyrightable material contained herein. This research used resources of beamlines 7-BM QAS, 28-ID 1 Pair Distribution Function (PDF), and 5-ID Submicron Resolution X-ray Spectroscopy (SRX) of the National Synchrotron Light Source II, a U.S. Department of Energy (DOE), Office of Science User Facility operated for the DOE Office of Science by Brookhaven National Laboratory under Contract No. DE-SC0012704. Christopher Tang is acknowledged for contributions to the pre-edge analysis of the vanadium XAS data. Esther S. Takeuchi acknowledges support as the William and Jane Knapp Chair in Energy and the Environment.

Conflict of Interest

The authors declare no conflict of interest.

Data Availability Statement

The data that support the findings of this study are available in the supplementary material of this article.

Keywords: aqueous battery · crystallite size · dissolution · sodium vanadium oxides · zinc-ion battery

- [1] B. Tang, L. Shan, S. Liang, J. Zhou, *Energy Environ. Sci.* **2019**, *12*, 3288.
- [2] J. Shin, J. Lee, Y. Park, J. W. Choi, *Chem. Sci.* **2020**, *11*, 2028.
- [3] P. Ruan, S. Liang, B. Lu, H. J. Fan, J. Zhou, *Angew. Chem.* **2022**, *134*, e202200598.
- [4] Y. L. Fan, Q. P. Wang, Y. Y. Xie, N. G. Zhou, Y. Yang, Y. C. Ding, Y. Wei, G. X. Qu, *Prog. Mater. Sci.* **2025**, *149*, 101393.
- [5] Y. Zhang, J. D. Howe, S. Ben-Yoseph, Y. Wu, N. Liu, *ACS Energy Lett.* **2021**, *6*, 404.
- [6] P. M. Marley, T. A. Abtew, K. E. Farley, G. A. Horrocks, R. V. Dennis, P. H. Zhang, S. Banerjee, *Chem. Sci.* **2015**, *6*, 1712.
- [7] A. Bergerud, R. Buonsanti, J. L. Jordan-Sweet, D. J. Milliron, *Chem. Mater.* **2013**, *25*, 3172.
- [8] L. W. Wangoh, Y. Q. Huang, R. L. Jezorek, A. B. Kehoe, G. W. Watson, F. Omenya, N. F. Quackenbush, N. A. Chernova, M. S. Whittingham, L. F. J. Piper, *ACS Appl. Mater. Interfaces* **2016**, *8*, 11532.
- [9] E. K. Suresh, B. Arun, J. Andrews, T. S. A. Raman, P. N. Mohan, C. Shivakumar, K. C. J. Raju, *Crit. Rev. Solid State Mater. Sci.* **2024**, *50*, 137.
- [10] M. Clites, J. L. Hart, M. L. Taheri, E. Pomerantseva, *ACS Energy Lett.* **2018**, *3*, 562.
- [11] P. Y. Zavalij, M. S. Whittingham, *Acta Crystallogr. Sect. B* **1999**, *55*, 627.
- [12] H. B. Li, F. M. Zhang, Q. L. Xian, L. Y. Yang, *Ionics* **2024**, *30*, 2697.
- [13] Y. Wang, X. Liu, G. B. Xu, Y. L. Liang, W. T. Ni, B. H. Wu, L. W. Yang, *Ionics* **2022**, *28*, 4709.
- [14] T. Zhou, A. B. Seethalakshmi, D. Arumugam, L. Zhang, A. M. M. Abeykoon, G. Kwon, D. Olds, X. Teng, *Chem. Mater.* **2024**, *36*, 11976.
- [15] H. Li, L. Zhu, W. Fan, Y. Xiao, J. Wu, H. Mi, F. Zhang, L. Yang, *CrystEngComm* **2025**, *27*, 191.
- [16] X. Y. Chen, J. H. Chen, Z. L. Wan, Y. Hu, D. R. Duan, Y. Zhao, Q. He, *Small* **2024**, *21*, 2406458.
- [17] S. J. Li, X. Y. Xu, K. Wang, W. X. Chen, X. Lu, Z. X. Song, J. Y. Hwang, J. Kim, Y. Bai, Y. Y. Liu, S. Xiong, *ACS Energy Lett.* **2022**, *7*, 3770.

- [18] S. J. Kim, C. R. Tang, G. Singh, L. M. Housel, S. Yang, K. J. Takeuchi, A. C. Marschilok, E. S. Takeuchi, Y. Zhu, *Chem. Mater.* **2020**, *32*, 2053.
- [19] C. R. Tang, G. Singh, L. M. Housel, S. J. Kim, C. D. Quilty, Y. Zhu, L. Wang, K. J. Takeuchi, E. S. Takeuchi, A. C. Marschilok, *Phys. Chem. Chem. Phys.* **2021**, *23*, 8607.
- [20] P. He, G. Zhang, X. Liao, M. Yan, X. Xu, Q. An, J. Liu, L. Mai, *Adv. Energy Mater.* **2018**, *8*, 1702463.
- [21] Z. Liu, H. Sun, L. Qin, X. Cao, J. Zhou, A. Pan, G. Fang, S. Liang, *ChemNanoMat* **2020**, *6*, 1553.
- [22] Y. Liu, X. Wu, *Nano Energy* **2021**, *86*, 106124.
- [23] Y. Dong, S. Deng, Z. Ma, G. Yin, C. Li, X. Yuan, H. Tan, J. Pan, L. Mai, F. Xia, *J. Mater. Sci. Technol.* **2022**, *121*, 80.
- [24] F. Wan, L. Zhang, X. Dai, X. Wang, Z. Niu, J. Chen, *Nat. Commun.* **2018**, *9*, 1656.
- [25] Y. Zhang, A. Chen, J. Sun, *J. Energy Chem.* **2021**, *54*, 655.
- [26] F. Wan, Z. Niu, *Angew. Chem.* **2019**, *131*, 16508.
- [27] Z. Xing, G. Xu, X. Xie, M. Chen, B. Lu, J. Zhou, S. Liang, *Nano Energy* **2021**, *90*, 106621.
- [28] X. Wang, B. Xi, X. Ma, Z. Feng, Y. Jia, J. Feng, Y. Qian, S. Xiong, *Nano Lett.* **2020**, *20*, 2899.
- [29] D. Zhang, J. Cao, Y. Yue, T. Pakornchote, T. Bovornratanarak, J. Han, X. Zhang, J. Qin, Y. Huang, *ACS Appl. Mater. Interfaces* **2021**, *13*, 38416.
- [30] L. Zhang, I. A. Rodríguez-Pérez, H. Jiang, C. Zhang, D. P. Leonard, Q. Guo, W. Wang, S. Han, L. Wang, X. Ji, *Adv. Funct. Mater.* **2019**, *29*, 1902653.
- [31] W. Li, C. Han, Q. Gu, S. L. Chou, J. Z. Wang, H. K. Liu, S. X. Dou, *Adv. Energy Mater.* **2020**, *10*, 2001852.
- [32] S. Liu, J. He, D.-S. Liu, M. Ye, Y. Zhang, Y. Qin, C. C. Li, *Energy Storage Mater.* **2022**, *49*, 93.
- [33] Y. Mei, Y. Liu, W. Xu, M. Zhang, Y. Dong, J. Qiu, *Chem. Eng. J.* **2023**, *452*, 139574.
- [34] H. Liu, L. Jiang, B. Cao, H. Du, H. Lu, Y. Ma, H. Wang, H. Guo, Q. Huang, B. Xu, *ACS Nano* **2022**, *16*, 14539.
- [35] B. Shuai, C. Zhou, Y. Pi, X. Xu, *ACS Appl. Energy Mater.* **2022**, *5*, 6139.
- [36] J. Guo, J. Ming, Y. Lei, W. Zhang, C. Xia, Y. Cui, H. N. Alshareef, *ACS Energy Lett.* **2019**, *4*, 2776.
- [37] J. L. Chen, W. L. Zhang, X. J. Zhang, Z. Y. Li, J. H. Ma, L. Zhao, W. B. Jian, S. L. Chen, J. Yin, X. L. Lin, Y. Qin, X. Qiu, *ChemSusChem* **2022**, *15*, e202200732.
- [38] Z. Zheng, J. Li, Y. Pan, Y. Yu, D. Zhu, J. Prabowo, L. Wei, Y. Chen, *Next Energy* **2023**, *1*, 100073.
- [39] Y. Xu, J. Zhu, J. Feng, Y. Wang, X. Wu, P. Ma, X. Zhang, G. Wang, X. Yan, *Energy Storage Mater.* **2021**, *38*, 299.
- [40] Z. Wang, M. Zhou, L. Qin, M. Chen, Z. Chen, S. Guo, L. Wang, G. Fang, S. Liang, *Escience* **2022**, *2*, 209.
- [41] S. Guo, L. Qin, T. Zhang, M. Zhou, J. Zhou, G. Fang, S. Liang, *Energy Storage Mater.* **2021**, *34*, 545.
- [42] S. Zafar, B. Lochab, *ACS Omega* **2024**, *9*, 47920.
- [43] J. E. Randles, *Trans. Faraday Soc.* **1948**, *44*, 327.
- [44] A. Sevcík, *Chem. Commun.* **1948**, *13*, 349.
- [45] A. Orita, M. Verde, M. Sakai, Y. Meng, *J. Power Sources* **2016**, *321*, 126.
- [46] Y. Shi, X. Zhou, J. Zhang, A. M. Bruck, A. C. Bond, A. C. Marschilok, K. J. Takeuchi, E. S. Takeuchi, G. Yu, *Nano Lett.* **2017**, *17*, 1906.
- [47] J. Wu, Z. Ju, X. Zhang, X. Xu, K. J. Takeuchi, A. C. Marschilok, E. S. Takeuchi, G. Yu, *ACS Nano* **2022**, *16*, 4805.
- [48] M. Onoda, *J. Phys.: Condens. Matter* **2004**, *16*, 8957.
- [49] H. Bachmann, W. Barnes, *Can. Mineral.* **1962**, *7*, 219.
- [50] G. Singh, C. R. Tang, A. Nicoll, J. Torres, L. M. Housel, L. Wang, K. J. Takeuchi, E. S. Takeuchi, A. C. Marschilok, *J. Phys. Chem. C Nanomater Interfaces* **2023**, *127*, 3940.
- [51] C. F. Bischoff, O. S. Fitz, J. Burns, M. Bauer, H. Gentischer, K. P. Birke, H. M. Henning, D. Biro, *J. Electrochem. Soc.* **2020**, *167*, 020545.
- [52] J. Wang, H. Huang, L. Qiao, H. Wang, K. Lee, G. Zhou, H. Liu, *J. Mater. Chem. A* **2024**, *12*, 31942.
- [53] X. Liu, X. Dong, S. Passerini, *J. Power Sources* **2024**, *623*, 235401.
- [54] Z. Liu, Y. Yang, S. Liang, B. Lu, J. Zhou, *Small Struct.* **2021**, *2*, 2100119.
- [55] R. Sahore, F. Dogan, I. D. Bloom, *Chem. Mater.* **2019**, *31*, 2884.
- [56] S. Klein, P. Bärmann, T. Beuse, K. Borzutzki, J. E. Frerichs, J. Kasnatscheew, M. Winter, T. Placke, *Chemsuschem* **2021**, *14*, 595.
- [57] G. A. Horrocks, L. R. De Jesus, J. L. Andrews, S. Banerjee, *JOM* **2017**, *69*, 1469.
- [58] D. C. Bock, A. C. Marschilok, K. J. Takeuchi, E. S. Takeuchi, *J. Power Sources* **2013**, *231*, 219.
- [59] A. A. Noyes, W. R. Whitney, *J. Am. Chem. Soc.* **1897**, *19*, 930.
- [60] Y. Hattori, Y. Haruna, M. Otsuka, *Colloids Surf. B: Biointerfaces* **2013**, *102*, 227.
- [61] Y. Shi, H. Zhou, I. D. Seymour, S. Britto, J. Rana, L. W. Wangoh, Y. Q. Huang, Q. Y. Yin, P. J. Reeves, M. Zuba, Y. Chung, F. Omenya, N. A. Chernova, G. Zhou, L. F. J. Piper, C. P. Grey, M. S. Whittingham, *ACS Omega* **2018**, *3*, 7310.
- [62] P. Chaurand, J. Rose, V. Bríois, M. Salome, O. Proux, V. Nassif, L. Oliví, J. Susini, J.-L. Hazemann, J.-Y. Bottero, *J. Phys. Chem. B* **2007**, *111*, 5101.
- [63] M. H. Alfaruqi, V. Mathew, J. Song, S. Kim, S. Islam, D. T. Pham, J. Jo, S. Kim, J. P. Baboo, Z. Xiu, *Chem. Mater.* **2017**, *29*, 1684.
- [64] G. Shulman, Y. Yafet, P. Eisenberger, W. Blumberg, *Proc. Natl. Acad. Sci.* **1976**, *73*, 1384.
- [65] H. Rietveld, *Acta Crystallogr.* **1967**, *22*, 151.
- [66] H. M. Rietveld, *J. Appl. Crystallogr.* **1969**, *2*, 65.
- [67] B. H. Toby, R. B. Von Dreele, *J. Appl. Crystallogr.* **2013**, *46*, 544.
- [68] L. Li, H. Yan, W. Xu, D. Yu, A. Heroux, W.-K. Lee, S. I. Campbell, Y. S. Chu, *PyXRF: Python-Based X-ray Fluorescence Analysis Package. In X-Ray Nanoimaging: Instruments And Methods III*, Vol. 10389, SPIE, USA **2017**, pp. 38–45.
- [69] B. Ravel, M. Newville, *J. Synchrotron Radiat.* **2005**, *12*, 537.
- [70] B. Ravel, M. Newville, *Phys. Scr.* **2005**, *2005*, 1007.

Manuscript received: January 16, 2025

Revised manuscript received: April 16, 2025

Version of record online: April 26, 2025